

# Formation of self-assembled asters in growing bacterial colonies

## Authors

Mustafa Başaran<sup>1,2\*</sup>, Y. Ilker Yaman<sup>1\*</sup>, Roman Vetter<sup>3,4</sup> and Askin Kocabas<sup>1,2,5,6†</sup>

<sup>1</sup>Department of Physics, Koç University, Sarıyer, Istanbul, Turkey 34450

<sup>2</sup>Bio-Medical Sciences and Engineering Program, Koç University, Sarıyer, Istanbul, Turkey 34450

<sup>3</sup>Computational Physics for Engineering Materials, ETH Zurich, 8093 Zurich, Switzerland

<sup>4</sup>Current address: Department of Biosystems Science and Engineering, ETH Zurich, 4058 Basel, Switzerland

<sup>5</sup>Koç University Surface Science and Technology Center, Koç University, Sarıyer, Istanbul, Turkey 34450

<sup>6</sup>Koç University Research Center for Translational Medicine, Koç University, Sarıyer, Istanbul, Turkey 34450

\*These authors contributed equally.

†Corresponding author: [akocabas@ku.edu.tr](mailto:akocabas@ku.edu.tr)

## Abstract

During colony growth, complex biomechanical interactions regulate the bacterial orientation, leading to the formation of large-scale ordered structures including topological defects. These structures may benefit bacterial strains, providing invasive advantages during colonization. Thus far, the emergence of  $\pm\frac{1}{2}$  topological defects has been observed and extensively assessed. Here, we experimentally and numerically investigate aster formation in bacterial colonies during inward growth when crowded populations invade a closed area. Herein, the velocity field and torque balance on the rod-shaped bacteria significantly differed, resulting in new stable orientational equilibrium in the radial direction and to the formation of +1 topological defects. The dynamics of these defects depend on bacterial length and can promote the survival of the longest bacteria around localized nutritional hot spots. The present results indicate a new mechanism underlying defect formation and provide mechanistic insights into the dynamics of bacterial growth on complex surfaces.

## Introduction

Bacterial colonization and invasion are collective phenomena. These processes are regulated through a complex interplay of physical and biological interactions in a crowded population. Bacterial morphology, hydrodynamics, surface topology, and topography markedly alter growth mechanisms, the morphology and overall competition among bacteria[1-6]. Elucidation of the factors regulating collective bacterial growth and their competition is essential to enhance our understanding of evolutionary dynamics, bacterial infection, and the progression of inflammatory diseases.

A characteristic feature of bacterial colonization is the formation of a large-scale order. Rod-shaped bacteria display nematic alignment on surfaces, wherein localized stress, surface friction, and elasticity trigger the formation of ordered domains and lead to the emergence of topological defects[7-11] and various types of self-assembled structures, including edge fingerings[12] and vertical structures[13, 14].

In particular,  $\pm \frac{1}{2}$  topological defects are the typical orientational singularities observed among growing bacterial colonies and biofilms[7, 9, 10, 15]. These topological defects have biological significance and regulate stress distribution across the structure and alter the physiology of the cells[16]; eventually, these effects trigger the formation of fruiting bodies[17] and bacterial spores in biofilms[15]. Liquid crystal theory has successfully predicted the dynamics of these defects;  $-\frac{1}{2}$  defects are stationary whereas  $+\frac{1}{2}$  defects are generally motile[18-20]. Another interesting structural order in bacterial colonies is active anchoring, where the bacteria are tangentially oriented along the edge of the colony[2, 7, 8].

In this study, we assess the orientational dynamics of a crowded bacterial population competing

for limited space. Unlike regular expanding colonies, if growing bacteria surround a closed area, domains of inward growth are formed. Under these conditions, entire mechanical interactions differ and lead to the formation of asters, formed as radially aligned +1 topological defects. Furthermore, we investigate the invasive advantages of radial orientation for competing bacterial strains of different lengths.

Inward growth is commonly observed in various biological systems. During wound healing, cancer cell growth, retina, and intestinal development, similar dynamic mechanisms are underway. Our results may provide novel mechanistic insights into these dynamics, particularly on the physical conditions for radial structural alignments during these complex growth processes.

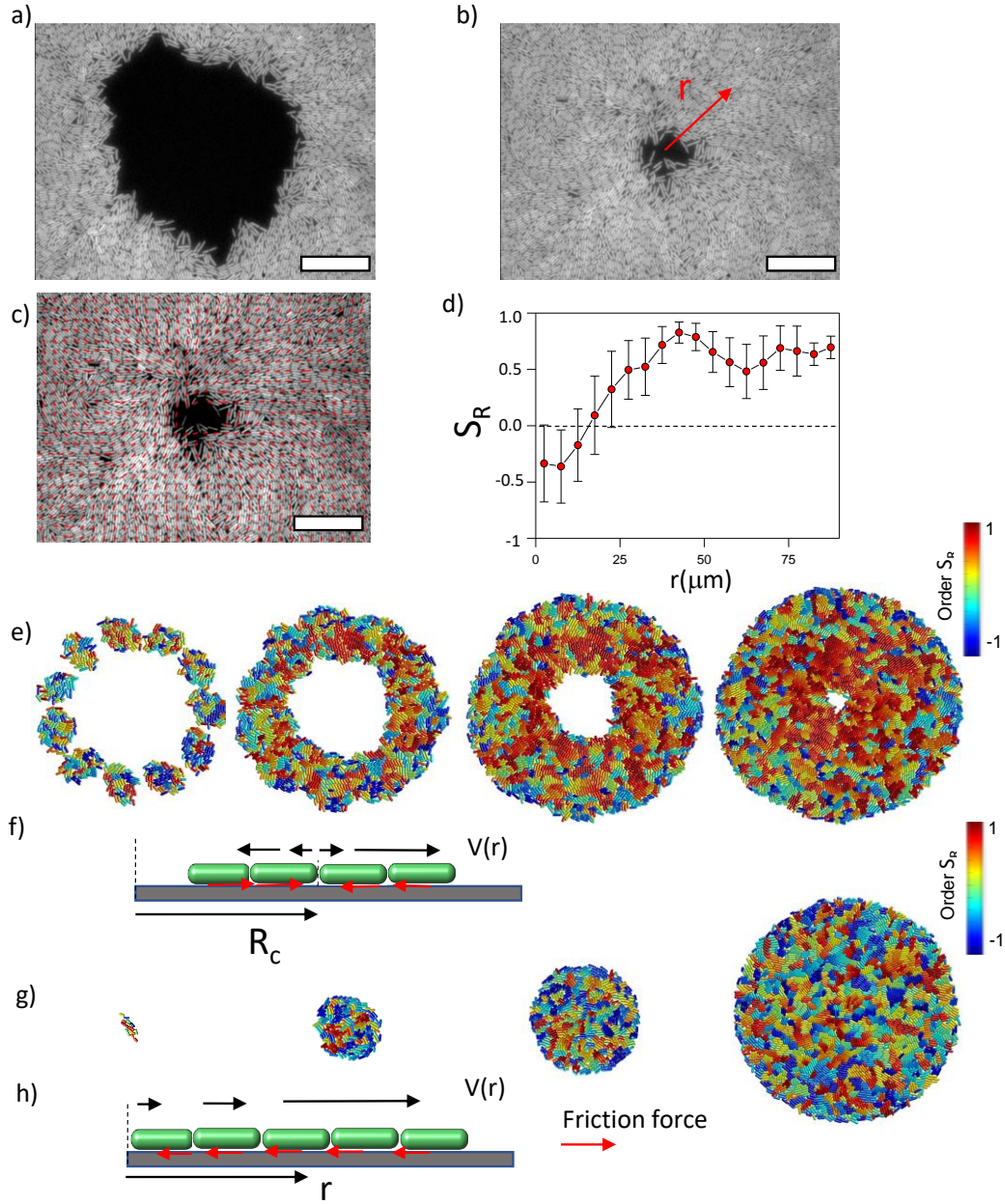


**Figure 1. Inward growth of bacterial colonies and emergence of asters.** **a)** Early stage of a closed area surrounded by growing bacterial colonies (*B. subtilis*). **b)** Snapshot of the radially aligned bacterial profile immediately before hole closure. **c)** A director field superimposed on an inward growing domain displaying radial alignment. Scale bar  $25\mu\text{m}$  **d)** The azimuthally averaged radial order parameter ( $S_R$ ) against the distance from the colony center for the colony snapshot given in (c). Error bars are defined as s.d. **e,g)** Simulation of 2D inward colony growth and regular expansion of bacterial colonies **f,h)** Schematic illustration of the velocity field (black arrow) and frictional force (red arrow) on bacteria in the inward and outward growing domain. Cell colors represent the radial order parameter ( $S_R$ ). Red represents radial alignment; blue, tangential alignment.

## RESULTS

To observe the dynamics of inward-growing bacterial colonies, we sparsely spread nonmotile *Escherichia coli* and *Bacillus subtilis* on a flat agarose surface (see Materials and Methods). Time-lapse fluorescence microscopy was then performed to investigate the temporal evolution of growing colonies. With colony growth, the closed area invaded by multiple colonies was observed across the plate. Rough colony interfaces gradually converge symmetrically, relatively smoothly, and enclosed circular areas. We refer to these shrinking circular regions as inward-growing bacterial domains because the growth direction is towards the center of the area. Figure 1 displays typical snapshots of the inward growth process (Fig. 1a, b, Supplementary Movie 1, 2). Unlike regular expanding colonies, the bacterial orientation around these domains is generally radial. To assess the orientation, we first analyzed the radial order parameter  $S_R$  around the center of these domains. The radial order parameter  $S_R$  can be expressed as:

$$\langle S_R \rangle = \frac{1}{N} \sum_i \cos [2(\theta^i - \phi^i)] \quad (1)$$

where  $\theta^i$  is the angular orientation with respect to x axis and  $\phi^i$  is the angular position of the bacterium  $i$  in polar coordinates about the colony center. Figure 1 d and c display the bacterial orientation and order parameter  $S_R(r)$  as a function of radial distance.  $S_R = +1$  corresponds to radial alignment and  $S_R = -1$  corresponds to tangential alignment. It is evident that large-scale radial order emerges across these inward growing domains (Fig. 1c, d).

To clarify differences in orientation between inward-growing and regular expanding colonies, we simulated 2D bacterial growth using molecular dynamics. We used the open-source simulation code GRO [21]. To determine the morphology of the inward growing domain, we initially

distributed bacteria in a random orientation. With bacterial growth, bacteria form small colonies which eventually fuse into a growing annulus (Fig. 1e). To visualize the large-scale order, we color-coded bacteria on the basis of their radial orientation, with red representing radial orientation, and blue representing tangential orientation around the center of the hole (Fig. 1e, Supplementary Movie 3). These simulation results captured the experimentally observed radial order across the colony.

However, regular expanding colonies only formed microdomains with random local orientations (Fig. 1g, Supplementary Movie 4). Regular expanding colonies represent the outward growth initiating from a single bacterium displayed in Figure 1g. Based on these simulations, the primary difference between regular expanding and inward-growing colonies is the sudden change in the direction of the surface friction force (Fig. 1f, h). In inward-growing colonies, this force flips its sign at a critical radius where the local radial velocity of the colony vanishes.

To further quantify the effects of the critical radius, we determined the stress distribution and radial velocity profile  $v_r$ , in growing colonies. Figure 2 summarizes the comparison and time evolution of these parameters. The stress is maximum around the critical radius during inward growth (Fig. 2a, b). As colonies grew, only inward-growing colonies developed substantial radial order  $S_R(r)$  (Fig. 2c, d). Furthermore, radial velocity profiles  $v_r$  significantly differed between regular expanding and inward-growing colonies. In contrast with regular expanding colonies, which have a linear radial velocity profile, inward-growing colonies developed radially nonlinear velocity which vanishes at the critical radius (Fig. 2e, f, Supplementary Fig. 1). Experimentally, similar profiles were measured (Supplementary Fig. 2). This profile gradually rotated the bacteria into the radial direction (Fig. 2g). Based on these results, the velocity profile appears to be the key physical parameter regulating the formation of the radial order.

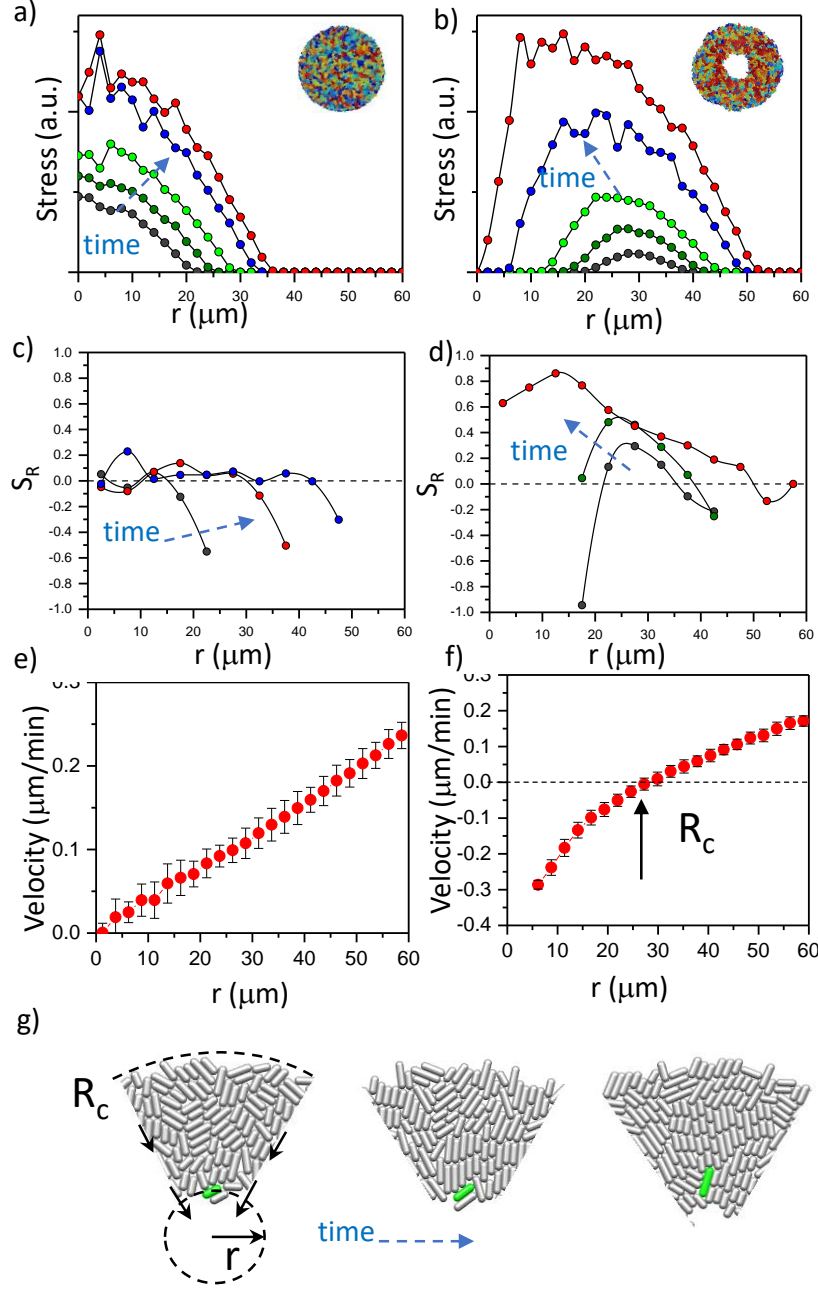


**Figure 2. Analysis of critical physical parameters during inward growth.** *a, b)* Plot of azimuthally averaged stress distribution at different time points of regular expanding and inward growing colonies against the distances from the center of the colony. *c, d)* Plot of azimuthally averaged radial order parameter ( $S_R$ ) across the colonies. Radial order emerges not only below the critical radius but also beyond this level. Negative radial order corresponds to a tangential orientation or active anchoring. *e, f)* Comparison of azimuthally averaged radial velocity ( $v_r$ ) profiles of regular expanding and inward-growing colonies. Regular expanding colonies display a linear profile; however, inward growing colonies form a nonlinear velocity profile. Error bars are defined as s.d. *g)* Snapshots of gradual rotation of a single bacterium (green) into a radial orientation during inward growth.



To better understand the association between the velocity profile on radial alignment, we first focused on the development of a minimum theoretical model based on active nematics. The theory of active nematics and liquid crystal physics provides a robust framework for understanding the dynamics of bacterial orientation. The primary characteristic of expanding colonies is the constant growth rate of the colony structure. The incompressibility criteria in 2D results in a linear relation between bacterial growth rate and radial velocity profile of the colony,  $v_r = g(r)r = \frac{\Lambda}{2}r$ , where  $g(r)$  is the local growth rate and  $\Lambda$  is the exponential bacterial growth rate. These coefficients are related for incompressible expanding bacterial colonies.

This relation was previously referred to as a Hubble-like constant owing to its similarity to the expansion of the universe[8]. We considered the same approximations to obtain insights into bacterial orientation during inward growth. First, we used the assumption that without molecular field and convection terms, the time evolution of the orientational angle  $\theta$  are simply regulated as follows(see Materials and Methods):

$$\frac{d\theta}{dt} = \frac{\xi g' r}{2S} \sin(2(\phi - \theta)) \quad (2)$$

where  $\phi$  is the angular position of the bacteria in polar coordinates, and  $\xi$  is the flow alignment parameter. Furthermore,  $g(r)$  is the local growth rate of the colony and its spatial derivative  $g'(r)$  regulating the stability of the bacterial orientation. The constant growth rate observed in regular expanding colonies does not provide any orientational preference,  $\frac{d\theta}{dt} = 0$ . However, this condition significantly differs during inward growth, wherein the local growth rate can be expressed as follows:

$$g(r) = \frac{v_r}{r} = \frac{\Lambda}{2} \frac{(r^2 - R_c^2)}{r^2} \text{ and } g'(r) = \Lambda \frac{R_c^2}{r^3} > 0 \quad (3)$$

Our assumption of a constant critical radius (Supplementary Fig. 1b) indicates that the spatial derivative of the growth rate is positive everywhere across the colony,  $g'(r) > 0$ , suggesting the possibility of a stable state with  $\theta = \phi$ . The stable radial orientation stimulates aster formation, being referred to as a +1 topological defect. This finding is significant because  $g'(r) > 0$  is generally possible in compressible structures. Although bacterial colonies are not compressible, inward growth and the shrinking hole structure alter the overall velocity profile and lead to an essential local growth rate.

The radial orientation is stable throughout the colony and not only below the critical radius. To clarify this point, we simulated colony growth under a fixed circular wall mimicking the stationary critical radius (Supplementary Fig. 3). We observed a similar radial alignment. These results indicate the association between the circular confinement owing to the critical radius and developed velocity profiles and the stability of bacterial orientations.

Thereafter, we investigated whether the same defects were obtained through the nemato-hydrodynamics equations of growing active matter[22, 23]. The continuum model is based on continuity, Navier–Stokes equations, and dynamics of the order parameter tensor  $\mathbf{Q}$ (see Materials and Methods). The coupled differential equations governing the primary material fields density  $\rho$ ,  $\mathbf{Q}$ , and velocity  $\mathbf{v}$  can be expressed as follows:

$$\frac{D\rho}{Dt} = \Lambda\rho + D_\rho \nabla^2 \rho \quad (4)$$

$$\frac{D(\rho\mathbf{v})}{Dt} = \nabla \cdot \boldsymbol{\sigma} - \gamma\rho\mathbf{v} \quad (5)$$

$$\frac{\partial \mathbf{Q}}{\partial t} + \mathbf{v} \cdot \nabla \mathbf{Q} = \xi \mathbf{u} + \mathbf{Q} \cdot \boldsymbol{\omega} - \boldsymbol{\omega} \cdot \mathbf{Q} + \Gamma^{-1} \mathbf{H} \quad (6)$$

Here,  $\frac{D}{Dt}$  is the material derivative, and the stress tensor is given as

$$\boldsymbol{\sigma} = -p\mathbf{I} - a(\rho)\mathbf{Q} - \xi\mathbf{H} + \mathbf{Q} \cdot \mathbf{H} - \mathbf{H} \cdot \mathbf{Q} \quad (7)$$

Here,  $a(\rho)\mathbf{Q}$  represents the active stress originating from the extensile nature of bacterial growth.  $\mathbf{u}$  and  $\boldsymbol{\omega}$  are the traceless strain and vorticity, respectively (see Materials and Methods). The critical parameter  $\xi$  is the flow alignment parameter. The details of the frictional drag coefficient per unit density  $\gamma$ , the molecular field  $\mathbf{H}$ , pressure  $p$ , rotational diffusion constant  $\Gamma$  and small diffusion coefficient  $D_\rho$  are given in Material and Methods. These equations were initially solved for growing bacterial colonies[3, 7, 8, 10, 24] and successfully predicted the active nematic nature and domain formations among colonies of rod-shaped bacteria. We solved them numerically with finite element method (FEM) (see Materials and Methods). As a benchmark, we compared the simulations with regular expanding colonies. Figure 3 summarizes the results of these continuum simulations. As expected, regular expanding colonies exhibited only local alignment (Fig. 3a, c, Supplementary Movie 5) corresponding to microdomains. However, inward-growing colonies developed robust radial alignment and order not only below but also beyond the critical radius (Fig. 3b, d, Supplementary Movie 6). Inward-growing colonies also displayed the expected nonlinear velocity profile required for radial alignment (Fig. 3e, f, Supplementary Movie 7, 8, Supplementary Fig. 4). Moreover, a sudden drop of the velocity profile near the inner and outer colony edges resulted in tangential orientation.

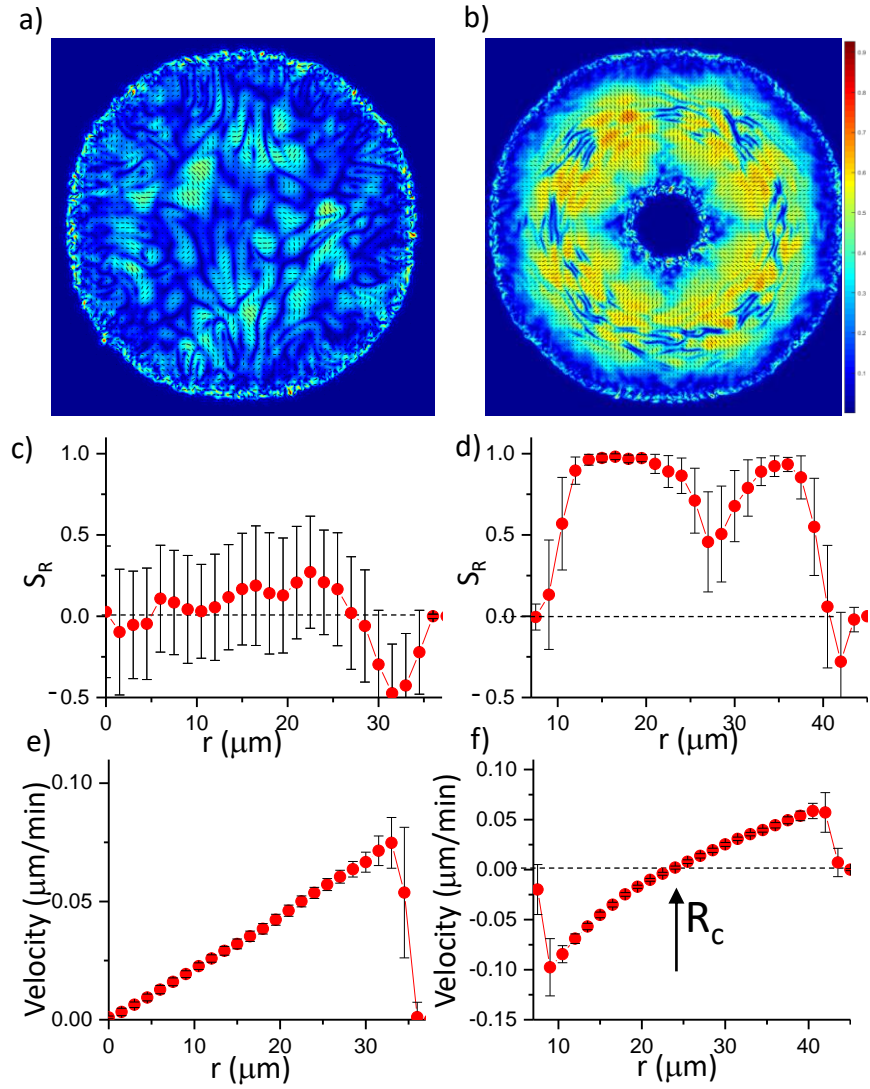


**Figure 3. Continuum simulations of 2D colony growth.** *a,b*) Scalar order parameter ( $S$ ) overlapped with the director field pattern of both regular expanding and inward-growing bacterial colonies. Comparison of azimuthally averaged *c,d*) radial order parameter ( $S_R$ ) and *e,f*) radial velocity ( $v_r$ ) profiles of the colonies against the distance from the center of the colony. In contrast with regular expanding colonies, inward-growing domains developed radial order throughout the colony. A sudden velocity drop near the edge of the colonies resulted in tangential orientation. Error bars are defined as s.d.

Herein, experimentally we only observed inward growing domains because the accumulated stress triggers multilayer formation (Supplementary Fig. 5). We investigated whether multilayered formation could change the radial alignment during inward growth by performing three-dimensional FEM simulations based on recently developed algorithms. The bacterial cells were modeled as growing elastic filaments that undergo controlled cell division during colony growth. Figure 4 shows the prototypical FEM simulation outcome from inward-growing colonies. As expected, accumulated stress triggers verticalization and multi-layer formation around the critical radius of the colony (Fig. 4a, b Supplementary Movie 9). However, a bacterial monolayer was also observed around the leading edge of the colony. This layer could also result in radial alignment during inward growth (Supplementary Movie 10). The width of the monolayer was approximately  $90\pm 30\mu m$  (Fig. 4c, d). This width defines the size of the aster structures observed herein.

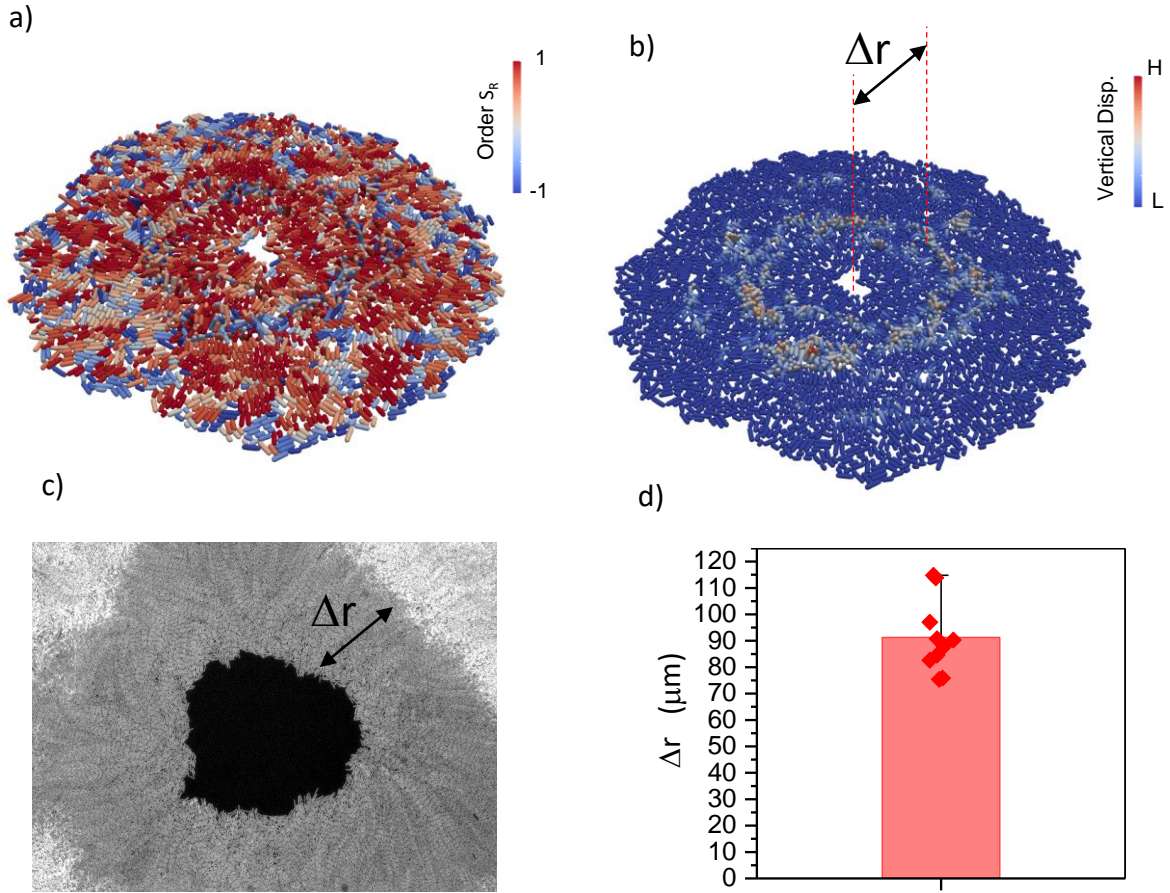


**Figure 4. 3D colony growth and multi-layer formation.** *a,b*) Snapshot of inward growing bacterial domains obtained through the finite element model simulation in 3D. The colors represent **(a)** the radial order parameter ( $S_R$ ) and **(b)** the vertical displacement of the bacteria during growth. **c**) Experimental snapshot of the inward-growing domain indicating the transition between mono- to multi-layer.  $\Delta r$  represents the width of the monolayer bacteria domain. **d**) Experimental data of  $\Delta r$  distribution. Error bars are defined as s.d.

Finally, to assess the biological significance of +1 topological defects, we investigated whether aster formation during inward growth potentially affect the competition among bacteria. In general, near the leading edge of a bacterial colony, competition strongly depends on physical parameters. The most prominent example is a genetic drift based on random fluctuations[25, 26]. This phenomenon could be altered through steric interactions among the cells, which can potentially alter the evolutionary dynamics of competing bacteria[27].

Although bacterial orientation is generally tangential at the expanding colony edge, radial bacterial alignment potentially contributes to inward growth. We hypothesized that rod-shaped bacteria potentially have an advantage owing to the torque balance. The basic premise is that the torque depends on the length of the bacteria, resulting in rapid radial alignment. Radial alignment further leads to lane formation and promotes an invasive advantage to the longest one, which could be beneficial in terms of approaching nutritional hotspots localized around the defect core more effectively.

To assess this competition, we initially simulated the growth dynamics of a mixed population with different division lengths from the same random initial distribution on a circle (Supplementary Fig. 5). Although the initial distribution of the bacteria is random, long bacteria can develop a higher radial order during inward growth (Fig. 5a-f). This radial order gradually allows the longest bacteria to approach the center of the defect more effectively (Fig. 5g). To visualize the advantage of radial alignment, we initially segregated the bacterial strain around the edge of the colony. Similar segregation can be commonly observed around the edge of the colony owing to random fluctuations. These segregations can also occur during inward growth (Supplementary Fig. 8). Instead of expanding segments owing to perimeter inflation, we observed shrinking segments owing to the deflation of the hole geometry. Computationally, the advantage of radial alignment was also evident in segregated bacterial colonies (Fig. 5h).

Interestingly, in a monolayer colony, radial alignment promotes the invasion of both the center and the leading outer edge of the colony through the longest bacteria (Fig. 5g). After complete invasion of the center, the radial lanes buckle (Supplementary Fig. 7, Supplementary Movie 11, 12). However, experimental verification of this competition remains challenging.

Although precise regulation of the aspect ratio of bacterial morphology is well established[28], cell length can still not be independently tuned without perturbing other essential physiological properties including growth rate and the biofilm-forming potential of the bacteria.

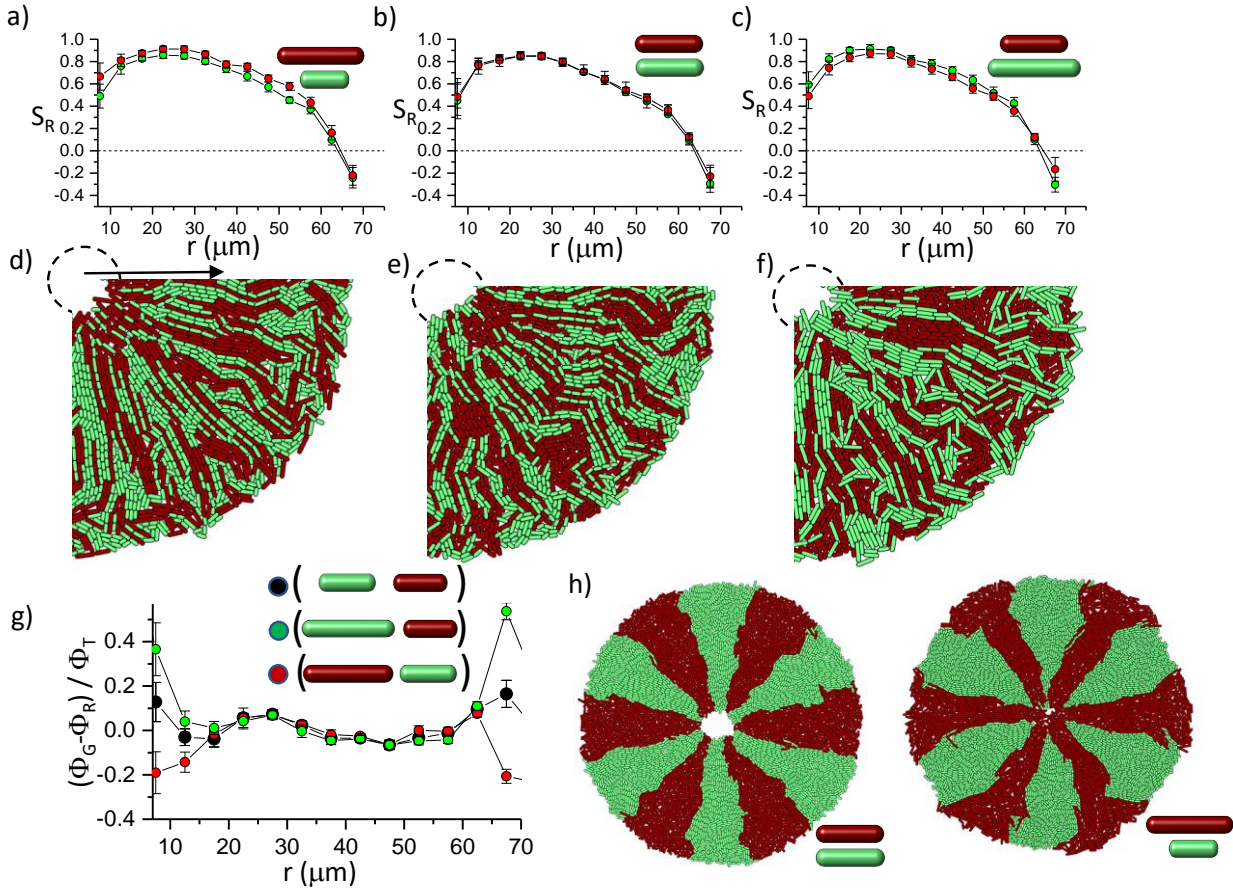


**Figure 5. Simulations of bacterial competition during inward growth.** *a,b,c)* Plot of the azimuthally averaged radial order parameter ( $S_R$ ) for green and red species against the distance from the colony center. Division lengths of green and red species are **(a)**  $L_{red} = 4.5 \mu m$ ,  $L_{green} = 3 \mu m$  **(b)**  $L_{red} = 3 \mu m$ ,  $L_{green} = 3 \mu m$  **(c)**  $L_{red} = 3 \mu m$ ,  $L_{green} = 4.5 \mu m$  **d, e, f)** Snapshot of multispecies simulations immediately before hole closure **(d)**  $L_{red} = 4.5 \mu m$ ,  $L_{green} = 3 \mu m$  **(e)**  $L_{red} = 3 \mu m$ ,  $L_{green} = 3 \mu m$  **(f)**  $L_{red} = 3 \mu m$ ,  $L_{green} = 4.5 \mu m$ . **(g)** Plot of relative packing fraction ( $(\Phi_{green} - \Phi_{red}) / (\Phi_{green} + \Phi_{red})$ ) as a function of distance from the center. **(h)** Simulation results of competing bacterial strains with equal and different division lengths immediately before hole closure. Long red bacteria form lanes and approach the center of the defect more efficiently. Error bars are defined as s.d.



## Discussion

Asters are ubiquitous topological structures observed in biological[29-32] or synthetic[33, 34] active matter systems. For instance, microtubules can form nematic alignment or asters during mitosis, depending on the extensile or contractile activity. Bacterial colonies can be considered an extensile active material platform, generally supporting the formation of  $\pm\frac{1}{2}$  topological defects. This study shows that aster structures can also emerge during inward growth. In particular, we report the critical role of the colony velocity profile during inward growth, which depends on numerous factors. Although the bacterial growth rate is constant throughout the colony, growth geometry, confinement, or boundary conditions can alter the velocity profile. Together, these biomechanical interactions change the bacterial orientation and stability, thus generating ordered structures. Different types of ordered structures have been observed in bacterial biofilms[35]. Furthermore, we believe that the velocity profile of biofilms growing on flat surfaces plays a significant role during biofilm alignment. Future studies are required to investigate the contribution of these effects. Finally, this study reveals the potential biological significance of topological defects during invasion. These ordered structures provide additional advantages and promote the survival of the longest bacteria. These results link the seemingly unrelated properties of topology and evolutionary dynamics of bacterial colonies. Our findings are of potential relevance for the understanding of complex dynamics of bacterial infections and the progression of inflammatory diseases.

## Methods

**Bacterial preparation and growth conditions.** Bacterial cultures (BAK47 and BAK51) were grown in Luria-Bertani (LB) broth at 37 °C on a shaker. An overnight culture was diluted 100x and grown for 8 h. The culture was diluted 10000x, and 10 µl of culture was seeded on an LB agarose plate. These isolated bacteria on plates were grown at 21 °C for 12 h and then imaged. The cover glass was kept on during imaging. Strains used in experiments are described in Table 1. In *B. Subtilis* bacterial strains, the flagella producing gene (*hag*) was mutated to eliminate the swimming induced motion. The background strain TMN1138 was obtained from R. Losick Lab.

**Microscopy imaging.** Fluorescence time-lapse imaging was performed using a Nikon inverted microscope and images were obtained using a Andor EMCCD camera. Time intervals between successive images are 5 minutes. Competing GFP and RFP labeled bacteria were circularly seeded on an agar plate using a cylindric sharp pipet.

**2D hard-rod simulations of growing colony.** We used open source simulation program GRO based on hard-rod model. We modified the original code to be able to change the initial bacterial position and using custom codes we extract the orientation of the bacteria to visualize the radial order.

**3D FEM simulations of growing bacterial colony.** For the 3D computer simulations, we employed a parallel finite element program written in C++[36]. Analogous to[15], the bacteria were modeled as an isotropic, linearly elastic continuum whose initial stress-free shapes were spherocylinders. The bacteria were assumed to maintain a uniform circular cross-section with radius  $r = 0.5\mu\text{m}$ , a mass density of  $1\text{gcm}^{-3}$ , a Young's modulus of  $E = 5300\text{Pa}$ , and a Poisson

ratio of  $\nu = 1/3$ . The total elastic energy  $\underline{U}$  of each bacterium comprised the usual terms for axial dilatation or compression, bending, and torsion[37]:

$$U = \frac{E\pi r^2}{2} \int_0^L \varepsilon^2 + \frac{r^2}{4} \left( \kappa^2 + \frac{1}{1+\nu} \varphi^2 \right) ds$$

where  $L$  denotes the bacterium length,  $\varepsilon$  the axial Cauchy strain,  $\kappa$  the scalar midline curvature, and  $\varphi$  the twist per unit length. Hertzian steric forces were exchanged between overlapping bacterial elements in normal direction. Tangential forces and torques exchanged during contact between bacterium pairs and between bacteria and the substrate were computed with a slip-stick friction model with a uniform isotropic Coulomb friction coefficient. We modeled the substrate as an elastic half-space onto which the bacterial colony was placed, and exerted a perpendicular gravitational force on the bacteria. The bacteria were grown exponentially in length over time by continuously increasing each element's equilibrium length. For this study, the finite element program was extended to allow for cell division when the bacterial length surpassed a division threshold  $L_\theta = 5\mu\text{m}$ . When  $L > L_\theta$ , the bacteria were split into two pieces at a random position drawn from a Normal distribution about their center with a standard deviation of  $L/10$ , but no further away from the center than  $L/5$ . To evolve the colony in time, Newton's translational and rotational equations of motion were integrated with a Newmark predictor-corrector method of second order. To equilibrate the colony during growth, viscous damping forces were added.

**Radial Velocity Profile.** To calculate radial velocity profile,  $v_r$ , during inward growth, we assume there is a critical radius  $R_c$ , where  $v_r$  is equals to zero. For  $r < R_c$  and the initial domain size equals to  $A_{in}$ :

$$A(t) = A_{in} e^{At} = \pi(R_c^2 - r^2) \quad (8)$$

If we take derivative wrt. time.

$$A_{in}\Lambda e^{\Lambda t} = -2\pi r \frac{dr}{dt} \quad (9)$$

$$v_r(r, t) = \frac{dr}{dt} = -\frac{\Lambda A(t)}{2\pi r} = \frac{\Lambda(r^2 - R_c^2)}{2r} \quad (10)$$

For outer growth where  $r > R_c$

$$A(t) = A_{out}e^{\Lambda t} = \pi(r^2 - R_c^2) \quad (11)$$

Similarly the time derivative is

$$A_{out}\Lambda e^{\Lambda t} = 2\pi r \frac{dr}{dt} \quad (12)$$

$$v_r(r, t) = \frac{dr}{dt} = \frac{\Lambda A(t)}{2\pi r} = \frac{\Lambda(r^2 - R_c^2)}{2r} \quad (13)$$

Which results the same equation. Consider that for  $r$  lower than  $R_c$ , velocity will be negative (inward direction) and for  $r$  greater than  $R_c$  velocity will be positive(outward direction).

**Continuum Modeling.** For the continuum modeling, Eq.4-7 were solved with the finite element method (FEM) in COMSOL Multiphysics. The material derivative is given by  $D/Dt = \partial_t + \mathbf{v} \cdot \nabla + (\nabla \cdot \mathbf{v})$ .  $\mathbf{u}$  and  $\mathbf{\omega}$  are the strain rate and vorticity tensors, respectively, with components  $u_{ij} = (\partial_i v_j + \partial_j v_i - \delta_{ij} \nabla \cdot \mathbf{v})/2$  and  $\omega_{ij} = (\partial_i v_j - \partial_j v_i)/2$ . We constructed traceless and symmetric Q-tensor field:

$$Q_{\alpha\beta} = S \left( n_\alpha n_\beta - \frac{1}{2} \delta_{\alpha\beta} \right) \quad (14)$$

and we defined scalar order parameter:

$$S(r) = \sqrt{2Q_{xx}^2(r) + 2Q_{xy}^2(r)} \quad (15)$$

The molecular field  $\mathbf{H}$  can be obtained starting from the Landau-de Gennes free energy density given as:

$$f_{LdG} = \frac{1}{2}K|\nabla \mathbf{Q}|^2 + \frac{1}{2}\alpha(\rho)\text{tr}[\mathbf{Q}^2] + \frac{1}{4}\beta(\rho)(\text{tr}[\mathbf{Q}^2])^2 \quad (16)$$

Therefore  $\mathbf{H} = \delta/\delta \mathbf{Q} \int dA f_{LdG} = K\nabla^2 \mathbf{Q} - \alpha(\rho)\mathbf{Q} - \beta(\rho)\text{tr}[\mathbf{Q}^2]\mathbf{Q}$ . In the simulations, the relationships  $a(\rho) = a_0\rho$ ,  $\beta(\rho) = \frac{\alpha_0}{2}\rho$ ,  $\alpha(\rho) = \alpha_0(\rho_c - \rho)$  and  $p = G * \max\left\{\left(\frac{\rho}{\rho_0} - 1\right), 0\right\}$  were used. We set the initial cell density  $\rho_0 = 1$ , growth rate  $\Lambda = 0.005$ , frictional drag coefficient per unit density  $\gamma = 0.2$ , flow aligning parameter  $\xi = 0.7$ , rotational diffusion constant  $\Gamma = 1$ , and the remaining parameters  $a_0 = 0.002$ ,  $\alpha_0 = 0.01$ ,  $\rho_c = \rho_0/2 = 0.5$ ,  $G = 2$ ,  $D_\rho = 0.04$ ,  $K = 0.01$ .

**Approximation for growth induced allignment.** The following approximation and equations are received from Dell’Arciprete et.al[8] for review process. The equation of motion for 2D nematodynamics without any free energy and no spatial variation of  $Q$  can be written as

$$\frac{\partial Q_{\alpha\beta}}{\partial t} + v_\gamma \partial_\gamma Q_{\alpha\beta} = \xi u_{\alpha\beta} - Q_{\alpha\gamma} \omega_{\gamma\beta} + \omega_{\alpha\gamma} Q_{\gamma\beta} \quad (17)$$

If we assume

$$v_r = g(r)r \quad (18)$$

From this formulation we can conclude that :

$$v_\alpha = g(r)x_\alpha \quad (19)$$

Where  $x_\alpha$  is the Cartesian component of the position vector

$$\partial_\beta v_\alpha = g\delta_{\alpha\beta} + g'rr_\alpha r_\beta \quad (20)$$

Where  $r_\alpha = \frac{x_\alpha}{r}$ . Now this tensor is symmetric, with calculating  $u_{\alpha\beta}$  and  $\omega_{\alpha\beta} = 0$  putting it in

(Eq. 17) above we get:

$$\frac{\partial Q_{\alpha\beta}}{\partial t} = \xi g' r \left( r_{\alpha} r_{\beta} - \frac{\delta_{\alpha\beta}}{2} \right) \quad (21)$$

With writing  $Q_{\alpha\beta}$  using :

$$Q_{\alpha\beta} = S \begin{bmatrix} \cos^2 \theta - \frac{1}{2} & \sin \theta \cos \theta \\ \sin \theta \cos \theta & \sin^2 \theta - \frac{1}{2} \end{bmatrix} \quad (22)$$

$$= \frac{S}{2} \begin{bmatrix} \cos(2\theta) & \sin(2\theta) \\ \sin(2\theta) & -\cos(2\theta) \end{bmatrix} \quad (23)$$

In polar coordinates  $(r, \phi)$  right hand side of (Eq. 21) is:

$$\frac{\partial Q}{\partial t} = \frac{\xi g' r}{2} \begin{bmatrix} \cos(2\phi) & \sin(2\phi) \\ \sin(2\phi) & -\cos(2\phi) \end{bmatrix} \quad (24)$$

If we combine (Eq.23) and (Eq.24):

$$-S \sin(2\theta) \frac{d\theta}{dt} = \frac{\xi g' r}{2} \cos(2\phi) \quad (25)$$

$$S \cos(2\theta) \frac{d\theta}{dt} = \frac{\xi g' r}{2} \sin(2\phi) \quad (26)$$

Multiply first equation(Eq.25) by  $-\sin(2\phi)$  and second equation(Eq.26) by  $\cos(2\phi)$  and sum them up:

$$\frac{d\theta}{dt} = \frac{\xi g' r}{2S} [\sin(2\phi) \cos(2\theta) - \cos(2\phi) \sin(2\theta)] \quad (27)$$

$$\frac{d\theta}{dt} = \frac{\xi g' r}{2S} \sin(2(\phi - \theta)) \quad (28)$$

Thus if  $g' > 0$  , equation above has a stable equilibrium for  $\theta = \phi$  (aster).

## Data Availability

All data supporting the findings in this study are available from the corresponding authors on request.

### Code Availability

All custom codes used in this study are available from the corresponding authors on request.

## References

### Acknowledgments

This work was supported by an EMBO installation Grant (IG 3275, A.K.) and BAGEP young investigator award (A.K.). We thank Sharad Ramanathan suggestions about bacterial competitions. We thank Julia Yeomans for discussions and suggestions. We thank F. M. Ramazanoglu for critical reading of the manuscript.

### Author contributions

Y.I.Y. , M.B and A.K. designed and performed experiments, analyzed data and developed the imaging systems. R.V. designed and developed the FEM simulation toolbox and optimized the codes with realistic bacterial parameters. M.B. performed the simulations. M.B. and A.K. prepared the draft, and all authors contributed to the final writing of the manuscript.

### Competing interests

Authors declare no competing interests.

## Tables

Strain	Parent	Operation	Genotype
BAK115	TMN1138	Transformed with plasmid ECE327 from Bacillus Genetic Stock Center	<i>amyE</i> ::Pveg-mKate (Spc) <i>sacA</i> ::P <sub>hag</sub> -mKate2L (Kan) <i>hagA233V</i> (Phleo)
BAK51	TMN1138	Transformed with plasmid ECE321 from Bacillus Genetic Stock Center	<i>amyE</i> ::Pveg-sfGFP (Spc) <i>sacA</i> ::P <sub>hag</sub> -mKate2L (Kan) <i>hagA233V</i> (Phleo)
BAK 55	DH5alpha	Transformed with plasmid 107741 from Addgene	<i>pDawn-sfGFP</i>

*Table 1: List of strains used in this study.*

1. Grant, M.A.A., et al., *The role of mechanical forces in the planar-to-bulk transition in growing Escherichia coli microcolonies*. Journal of the Royal Society Interface, 2014. **11**(97).
2. Su, P.T., et al., *Bacterial Colony from Two-Dimensional Division to Three-Dimensional Development*. Plos One, 2012. **7**(11).
3. Volfson, D., et al., *Biomechanical ordering of dense cell populations*. Proceedings of the National Academy of Sciences of the United States of America, 2008. **105**(40): p. 15346-15351.
4. Warren, M.R., et al., *Spatiotemporal establishment of dense bacterial colonies growing on hard agar*. Elife, 2019. **8**.
5. Cho, H.J., et al., *Self-organization in high-density bacterial colonies: Efficient crowd control*. Plos Biology, 2007. **5**(11): p. 2614-2623.
6. Smith, W.P.J., et al., *Cell morphology drives spatial patterning in microbial communities*. Proceedings of the National Academy of Sciences of the United States of America, 2017. **114**(3): p. E280-E286.
7. Doostmohammadi, A., S.P. Thampi, and J.M. Yeomans, *Defect-Mediated Morphologies in Growing Cell Colonies*. Physical Review Letters, 2016. **117**(4).
8. Dell'Arciprete, D., et al., *A growing bacterial colony in two dimensions as an active nematic*. Nature Communications, 2018. **9**.
9. Doostmohammadi, A., et al., *Active nematics*. Nature Communications, 2018. **9**.
10. You, Z.H., et al., *Geometry and Mechanics of Microdomains in Growing Bacterial Colonies*. Physical Review X, 2018. **8**(3).
11. You, Z., D.J.G. Pearce, and L.J.a.e.-p. Giomi *Confinement-induced self-organization in growing bacterial colonies*. 2020. arXiv:2004.14890.
12. Farrell, F.D.C., et al., *Mechanically Driven Growth of Quasi-Two-Dimensional Microbial Colonies*. Physical Review Letters, 2013. **111**(16).
13. Beroz, F., et al., *Verticalization of bacterial biofilms*. Nature Physics, 2018. **14**(9): p. 954-+.
14. Hartmann, R., et al., *Emergence of three-dimensional order and structure in growing biofilms*. Nature Physics, 2019. **15**(3): p. 251-+.
15. Yaman, Y.I., et al., *Emergence of active nematics in chaining bacterial biofilms*. Nature Communications, 2019. **10**.
16. Saw, T.B., et al., *Topological defects in epithelia govern cell death and extrusion*. Nature, 2017. **544**(7649): p. 212-+.
17. Copenhagen, K., et al. *Topological defects induce layer formation in Myxococcus xanthus colonies*. 2020. arXiv:2001.03804.
18. Shankar, S. and M.C. Marchetti, *Hydrodynamics of Active Defects: From Order to Chaos to Defect Ordering*. Physical Review X, 2019. **9**(4).
19. DeCamp, S.J., et al., *Orientational order of motile defects in active nematics*. Nature Materials, 2015. **14**(11): p. 1110-1115.
20. Giomi, L., et al., *Defect Annihilation and Proliferation in Active Nematics*. Physical Review Letters, 2013. **110**(22).
21. Jang, S.S., et al., *Specification and Simulation of Synthetic Multicelled Behaviors*. Acs Synthetic Biology, 2012. **1**(8): p. 365-374.
22. Giomi, L., et al., *Banding, excitability and chaos in active nematic suspensions*. Nonlinearity, 2012. **25**(8): p. 2245-2269.
23. Olmsted, P.D. and P.M. Goldbart, *Isotropic-Nematic Transition in Shear-Flow - State Selection, Coexistence, Phase-Transitions, and Critical-Behavior*. Physical Review A, 1992. **46**(8): p. 4966-4993.
24. Atis, S., et al., *Microbial Range Expansions on Liquid Substrates*. Physical Review X, 2019. **9**(2).
25. Hallatschek, O., et al., *Genetic drift at expanding frontiers promotes gene segregation*. Proceedings of the National Academy of Sciences of the United States of America, 2007. **104**(50): p. 19926-19930.
26. Kayser, J., et al., *Emergence of evolutionary driving forces in pattern-forming microbial populations*. Philosophical Transactions of the Royal Society B-Biological Sciences, 2018. **373**(1747).
27. Farrell, F.D., et al., *Mechanical interactions in bacterial colonies and the surfing probability of beneficial mutations*. Journal of the Royal Society Interface, 2017. **14**(131).
28. Dion, M.F., et al., *Bacillus subtilis cell diameter is determined by the opposing actions of two distinct cell wall synthetic systems*. Nature Microbiology, 2019. **4**(8): p. 1294-1305.
29. Roostalu, J., et al., *Determinants of Polar versus Nematic Organization in Networks of Dynamic Microtubules and Mitotic Motors*. Cell, 2018. **175**(3): p. 796-+.
30. Ross, T.D., et al., *Controlling organization and forces in active matter through optically defined boundaries*. Nature, 2019. **572**(7768): p. 224-+.
31. Kruse, K., et al., *Asters, vortices, and rotating spirals in active gels of polar filaments*. Physical Review Letters, 2004. **92**(7).



32. Julicher, F., et al., *Active behavior of the cytoskeleton*. Physics Reports-Review Section of Physics Letters, 2007. **449**(1-3): p. 3-28.
33. Sokolov, A., et al., *Emergence of Radial Tree of Bend Stripes in Active Nematics*. Physical Review X, 2019. **9**(3).
34. Snezhko, A. and I.S. Aranson, *Magnetic manipulation of self-assembled colloidal asters*. Nature Materials, 2011. **10**(9): p. 698-703.
35. Yan, J., et al., *Vibrio cholerae biofilm growth program and architecture revealed by single-cell live imaging*. Proceedings of the National Academy of Sciences of the United States of America, 2016. **113**(36): p. E5337-E5343.
36. Vetter, R., et al., *Finite element simulation of dense wire packings*. European Journal of Mechanics a-Solids, 2013. **37**: p. 160-171.
37. Vetter, R., F.K. Wittel, and H.J. Herrmann, *Packing of elastic wires in flexible shells*. Epl, 2015. **112**(4).

### **Supplementary Video Captions:**

**Movie 1-** Radial alignment during inward growth and emergence of asters. The video shows the fluorescence image of GFP labeled *E.coli* (BAK 55) during inward growth.

**Movie 2-** Radial alignment during inward growth and emergence of asters. The video shows the second example of fluorescence image of GFP labeled *B. Subtilis* strain (BAK 51) during inward growth. This video is associated with Figure 1a-d

**Movie 3** 2D Simulation of bacterial colony during inward growth. This video is associated with Figure 1f.

**Movie 4** 2D Simulation of bacterial colony during regular expansion. This video is associated with Figure 1g.

**Movie 5** Continuum simulation of 2D colony growth during regular expansion. Scalar order parameter is overlapped with director field pattern. This video is associated with Figure 3a.

**Movie 6** Continuum simulation of 2D colony growth during inward growth. Scalar order parameter is overlapped with director field pattern. This video is associated with Figure 3b.

**Movie 7** Continuum simulation of 2D colony growth during regular expansion. Colony density is overlapped with velocity field pattern. This video is associated with Figure 3e.

**Movie 8** Continuum simulation of 2D colony growth during inward growth. Colony density is overlapped with velocity field pattern. This video is associated with Figure 3f .

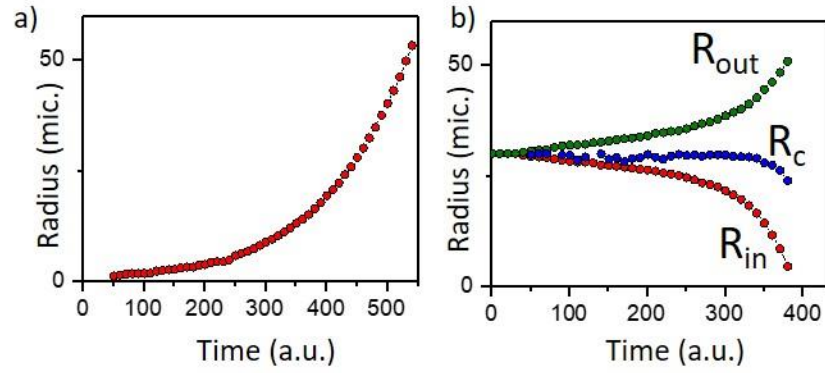
**Movie 9** 3D FEM simulation of colony growth during inward growth. Color represents the vertical displacement. This video is associated with Figure 4b .

**Movie 10** 3D FEM simulation of colony growth during inward growth. Color represents the radial order parameter. This video is associated with Figure 4a .

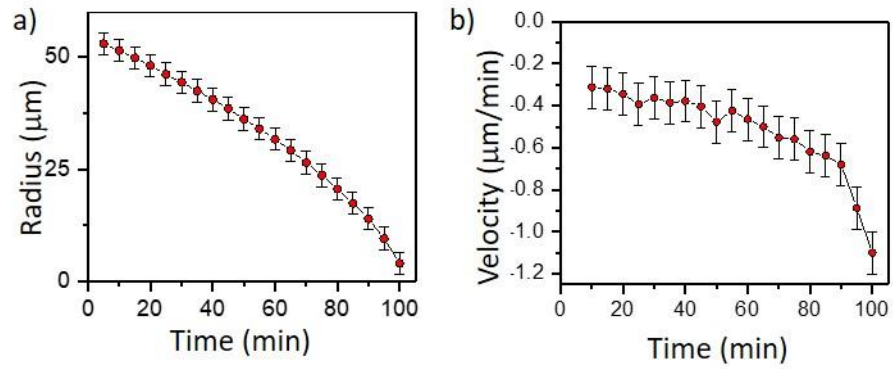
**Movie 11** 2D simulation results of competing bacterial strains with identical division lengths. RFP and GFP labeled bacteria are initially segregated. Color represents the bacterial type. This video is associated with Figure 5h .

**Movie 12** 2D simulation results of competing bacterial strains with different division lengths. RFP and GFP labeled bacteria are initially segregated. Color represents the bacterial type. This video is associated with Figure 5h .

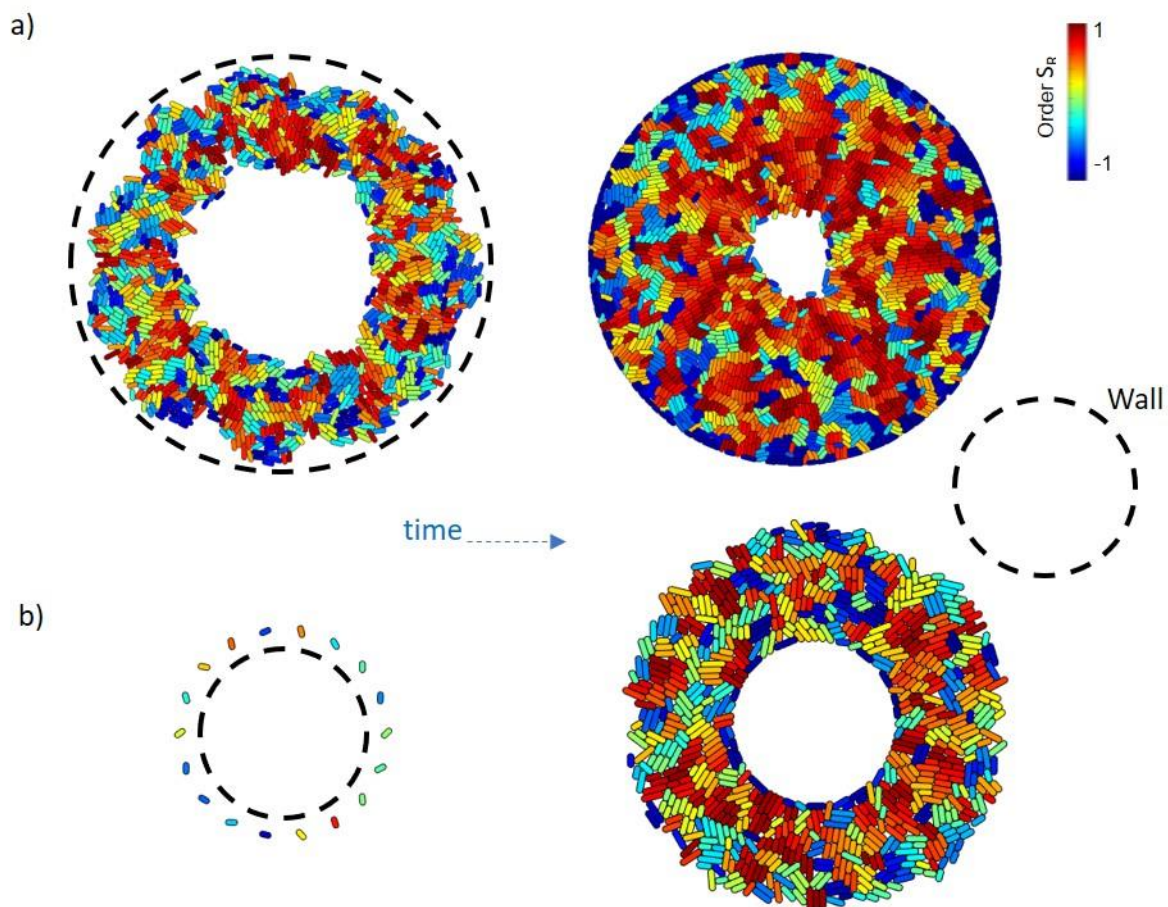
**Supplementary Figures:**



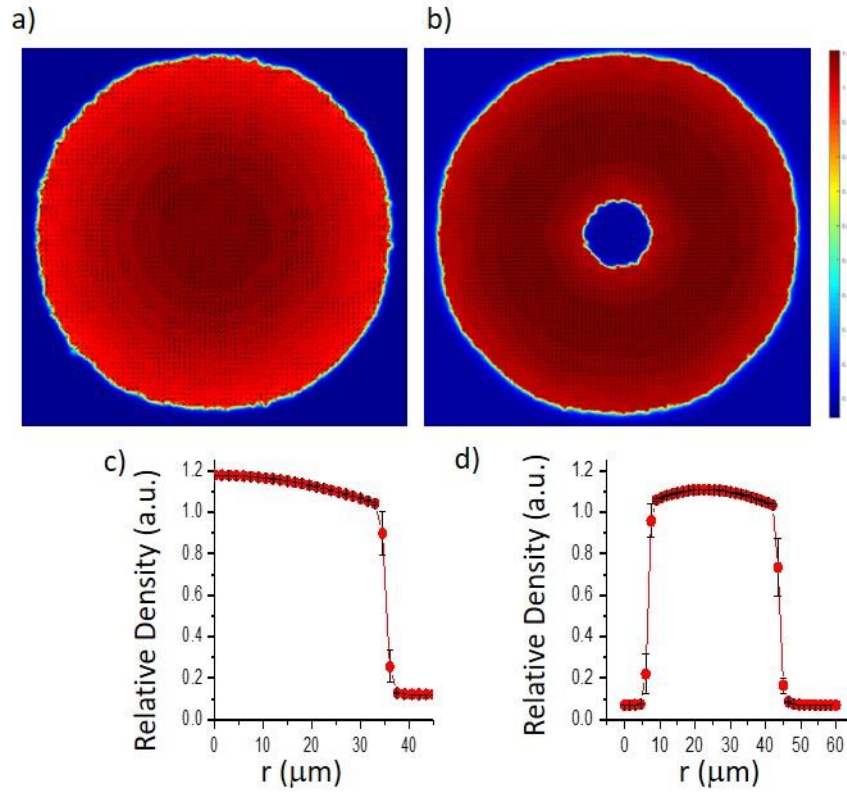
**Supplementary Fig. 1** Molecular dynamics simulations of colony radius. **a)** Plot of radius of bacterial colony of regular expanding colony against time. **b)** Plot of inner and outer radius of bacterial colony of inward growing colony against time. Critical radius is determined by where  $v_r$  equals to zero. Critical radius shows constant profile immediately before hole closure.



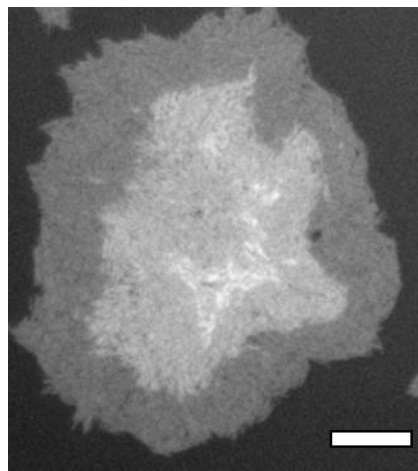
**Supplementary Fig. 2** . Experimental measurements of velocity profile. **a)** Plot of inner radius of inward growing bacterial domain against time. **b)** Plot of radial velocity ( $v_r$ ) of inner edge of inward growing bacterial domain in the experiment against time.



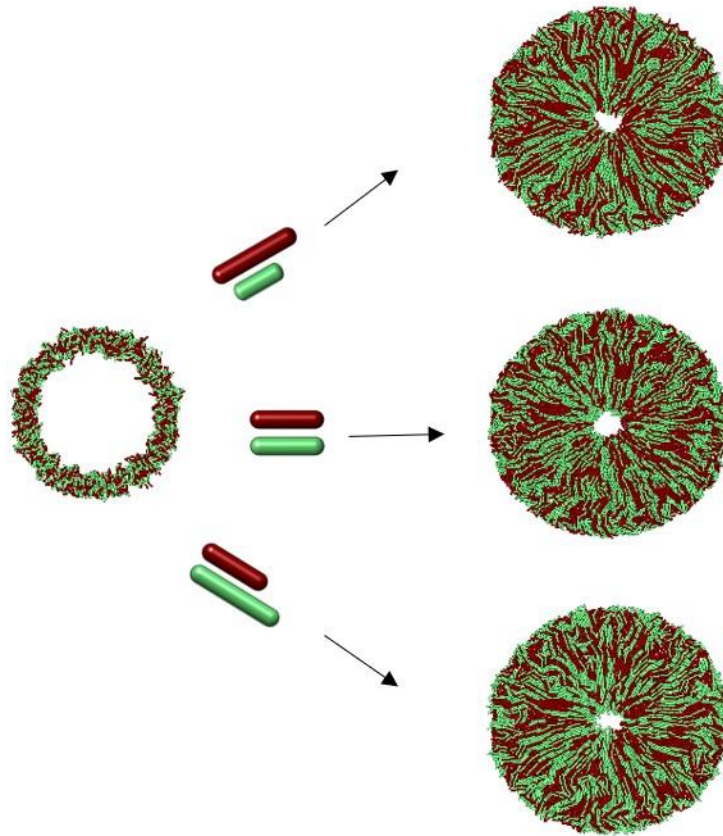
**Supplementary Fig. 3** Simulation results of growing bacterial colony under circular confinement defined by a fixed wall. Under both conditions colonies can develop radial alignment.



**Supplementary Fig. 4 .** Continuum simulation results of colony density and velocity profiles . **a,b)** velocity field superimposed on a density profile of regular expanding and inward growing colony. **c,d)** Plot of azimuthally-averaged density against the distance from the colony center for regular expanding and inward growing colony

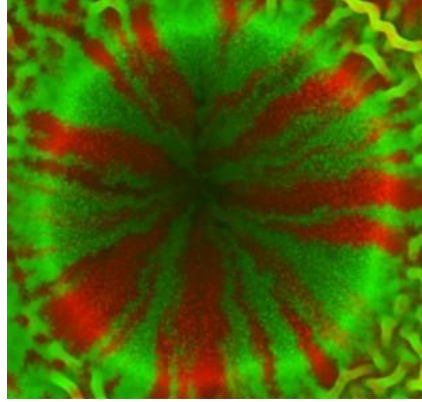


**Supplementary Fig. 5** Formation of multi layered colony structures. Bright regions around the center correspond to the second and the third layers. Scale bar corresponds to 100  $\mu\text{m}$ .



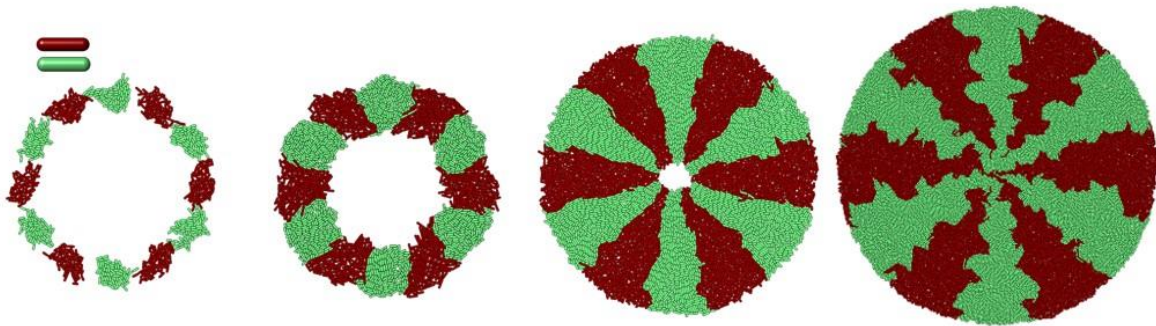
**Supplementary Fig. 6** 2D simulation results of competing bacterial strains with different division lengths. Starting from random initial annulus distribution, longest bacteria could develop higher radial order.



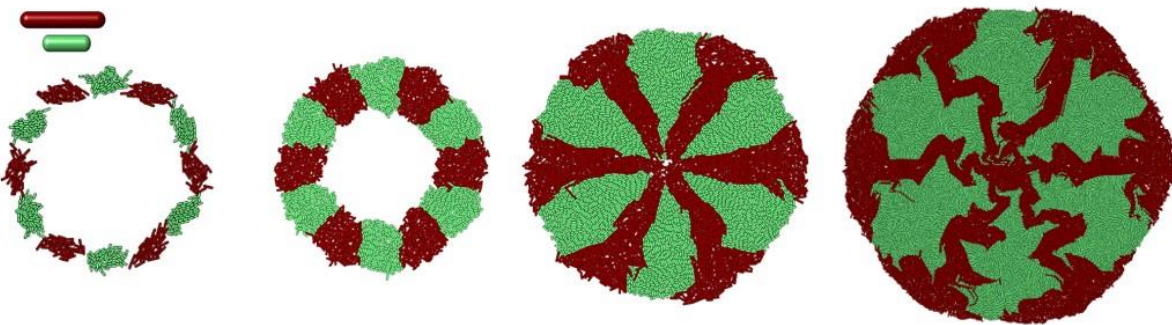


**Supplementary Fig. 7** Experimental verification of bacterial segregation due to random fluctuation during inward growth. Competing RFP and GFP labeled, identical bacterial strains were mixed and printed on an agar surface using cylindrical sharp object.

a)



b)



**Supplementary Fig. 8** Simulation results of competition of segregated bacterial strains. Longest bacteria can invade the center more effectively.